CHAPTER 2. EXPERIMENTAL METHODS

As we argued in Chapter 1, the ideal experimental approach that completely isolates small droplets is through electrodynamic balance (EDB). However, to implement this method and obtain useful results requires several subsystems of the experimental apparatus. These subsystems include: charged droplet generation, droplet injection, droplet levitation, and visualization. In this Chapter we discuss the theory and implementation of components of the experimental apparatus and show how they work together to lend us the powerful tool to investigate the evaporation of sub-100 micron droplets elevated by electrostatic force,

2.1 Droplet generation

Many conventional droplet generation methods rely on the microdispening of liquids by a syringe and hypodermic needle (Gan, 2011; Imanura, 2005 and Nesic, 1991). This approach limits the droplet size to be comparable with the capillary length $L_c \sim (\gamma/\rho g)^{1/2}$, where γ is the surface tension, ρ is the liquid density, and g is the gravitation constant. Typical liquids have a capillary length of ~1mm, which makes the droplet size too large for our investigation due to the potential complication brought by internal circulation. On the other hand, many applications of interests, such as in internal combustion engines, the droplets size are usually around 100 μm to increase combustion efficiency and reduce pollution emissions..

To generate sub-100 μm droplets, one mature and popular technique is inkjet. The inkjet head uses a short pressure pulse generated either thermally or piezoelectrically to expel one or more ~100 picoliter liquid droplets out of a nozzle (typically about 30 μm in

orifice diameter to avoid frequent clogging). The working principle of inkjet may impose several restrictions on the type of suspension and solution it can handle. For example, the IJP limits the liquid viscosity to 20 mPa (Holland, 1983). Also, the droplet diameter generated by inkjet is > 10 μm because the inertia based atomization requires the droplet size to be comparable to nozzle inner diameter.

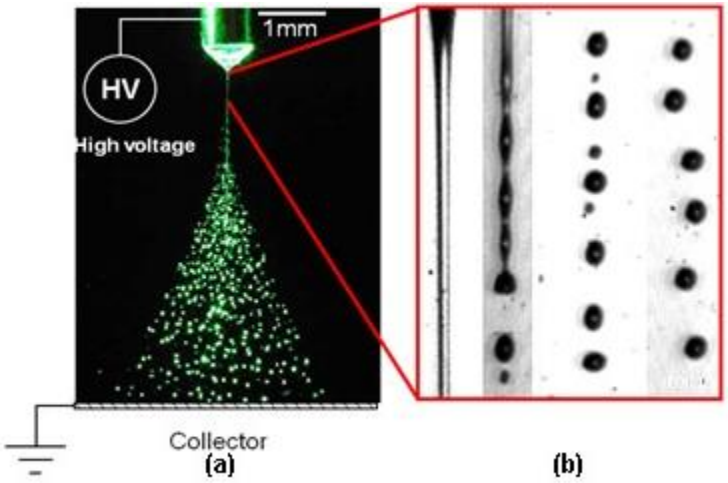

Figure 1 (a) Electrospray atomizer; (b) ordered breakup

One atomizer that can achieve both quasi-monodisperse and small (<100 μm) droplets is electrospray. Electrospray is the liquid atomization principle behind the 2002 Nobel Chemistry Prize recognizing Prof. John Fenn's contribution to the electrospray ionization mass spectroscopy (ESI-MS) (Fenn, 1989). Compared to other techniques discussed above, *ES* has the unmatched capability of producing monodispersed droplets in the few nm to 10 μm range (Almeria, 2014). A typical *ES* system (Fig. 4) is implemented by feeding a liquid with high electric conductivity (such as deionized water) through a tube which is charged to a few kV. The liquid at the nozzle tip has several different operation modes (Yang, 2012). Among these modes, the most widely used and studied one is the *cone-*

jet mode (Ganan-Calvo, 1997; Hartman, 2000). There, the liquid takes a conical shape (named Taylor-cone (Taylor, 1964)) resulting from the balance of surface tension and electric *norm* stress. The electric *shear* stress drives and accelerates the liquid at the liquid surface, from nearly zero velocity at the base of the cone to >10m/s at the apex of the cone (Wilhelm, 2004; Duff, 2003). This unique jetting mechanism eliminates liquid-solid friction which leads to low-pressure drop and a minimum risk of clogging.

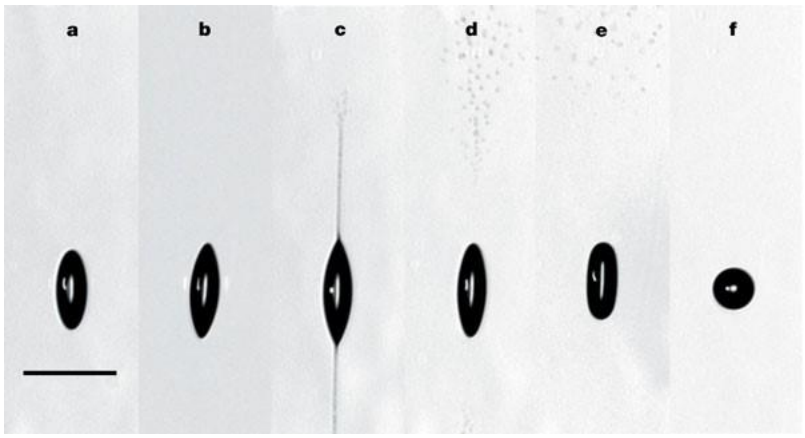

Figure 2 Coulomb fission of a charged droplet. (Duft, 2003)

It is worth noticing that during the evaporation process the surface charge density is increased due to the decreasing droplet diameter. Once the charge density reaches or surpasses a threshold at which the cohesive force as a result for the surface tension equals or smaller than the repulsive electrostatic force, the droplet becomes unstable. The unstability leads to droplet breakup and progency droplets are formed, which is referred to Coulombic fission.

It is preferable that droplet can stay as long as possible before it explodes. Rayleigh, 1882 first analyzed the stability of a charged droplet. According to his theory the instability

of a droplet occurs when the charge on the droplet reaches a critical value, which is expressed as

$$q_R = 8\pi\sqrt{\varepsilon_0 \gamma a^3} \tag{2.1}$$

where ε_0 is the permittivity constant, γ is the surface tension of the droplet, and a is the droplet radius. Eq. (2.1) shows the charge limit of a droplet decreases as droplet size decreases.

Consider a droplet with the initial size of a_0 and charge of q_0. The Rayleigh limit can be expressed as

$$q_{R0} = 8\pi\sqrt{\varepsilon_0 \gamma a_0^3} \tag{2.2}$$

Assume the droplet charge reaches Rayleigh limit when the radius decreases to a,

$$q_0 = 8\pi\sqrt{\varepsilon_0 \gamma a^3} \tag{2.3}$$

Then we have

$$\frac{q_0}{q_{R0}} = \left(\frac{a}{a_0}\right)^{3/2} \tag{2.4}$$

where q_0 / q_{R0} is defined as charge ratio. If we would like to the study the evaporation process from beginning to 10% of the initial size, the charge of the droplet needs to be less than 3% of the Rayleigh limit. The charge ratio of droplets under cone jet mode is around 70%. The value gradually decreases under pulsing mode and dripping mode. Therefore the ES will be performed under dripping mode and pulsing mode to reduce the initial charge ratio.

2.2 Droplet injection

There are two issues with using electrospray atomization for levitation. First, the electrospray process generates droplets at very high rate (~100,000 droplets/second), which are way more than we need. Second, the velocity of the droplets is too high (~10m/s) for the levitation device to be discussed in Section 2.3. Therefore, the droplet injection component will serve two functions: firstly to serve as a filter and shutter, and secondly to decelerate the droplet to the velocity of ~5cm/second.

Figure 7 illustrates the design of the droplet injection component. It mainly consists of two flat parallel metal plates with small holes at the center. The top plate functions as the first filter of droplets, as the area of the hole is only 1/1000 of the footprint of the electrospray. The second plate will further filter excess droplets. A simple mechanical shutter is placed on top of the top plate that allows manual open and block of the first injection hole. By opening the shutter for a few seconds, a charged droplet will pass both holes and reaches the levitator.

In addition, the DC electric field is established between the two plates which slow down the charged droplets. The potential difference between the two plates is slightly smaller than the voltage required for generating electrospray. This makes sense because the electrospray is a very efficient process which convert majority of the electric potential energy into liquid droplets' kinetic energy during the atomization phase; while during the injection process the droplets lose nearly all kinetic energy (99%) in penetrating the electric potential barrier.

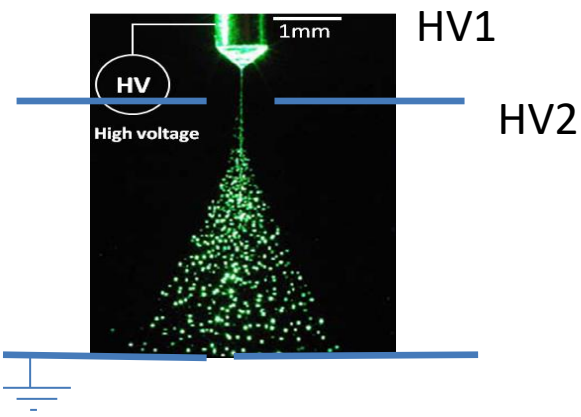

Figure 3: Design of the droplet injection component

2.3 Electrodynamic Balance Levitation System

We use the electro-dynamic balance (EDB) which is capable of levitating droplet diameters of a few tens or micrometers (Shaw, 2000; Davis, 1980; Agnes, 2002) that is desirable for investigating both diffusion-rate controlled and kinetically controlled evaporation regime (Davis, 1980). To use EDB, the droplet would have to carry electric charges, which requires integrating the capability of adding electric charges to droplets with droplet generation. The combination of EDB and ES provides an effective tool suited for the study of the evaporation and burning characteristics of fuel nanofluid droplets. Droplets thus generated carry static electric charges and, when placed in a properly design electric field as that using EDB, can be suspended immediately followed by experimental probing prior to significant evaporation (this is especially notable as the D^2-law indicates that smaller droplets evaporate faster than larger droplets).

EDB is developed based on the quadrupole mass filter that is proposed by Paul and Steinwedel (1953). A charged particles suspended by means of the electrical fields. The

device can trap particles with the size range of nanometer to hundreds of micrometer by adjusting the AC frequency and magnitude.

Many configurations have been developed according to specific application. Wuerker (1959) introduced the bihyperboloidal electrode configuration to trap ion. Straubel(1959) developed a relatively simple configuration consisting of an AC ring electrode placed in the middle of DC planes. Maloney, 1995 developed a modified version of EDB to measure the trajectories and drag force characteristic of individual particles. A simple form of electrodynamic balance with the double ring geometry was analyzed by Davis, 1990. Zheng, 2001 also introduced a double ring device to achieve control of a particle in three dimensions.

In all these electrode configurations, the oscillatory forces that is exerted by the AC filed to trap the particle. The DC field applied is used to balance the gravitational force and any other vertical forces on the particle.

2.3.1 Theory of classic bihyperboloidal EDB device

The classic bihyperboloidal configuration includes hyperboloidal endcap electrodes and a central ring electrode. The ac voltage is applied to the ring electrode to achieve the focusing. The endcaps are connected to dc voltages to introduce upward electrical force and the distribution of the positive and negative potential is adjusted according to the polarity of the charged particle. If the particle has positive charge, the positive voltage should be applied on the bottom endcap and negative voltage should be connected to the top endcap and vice versa.

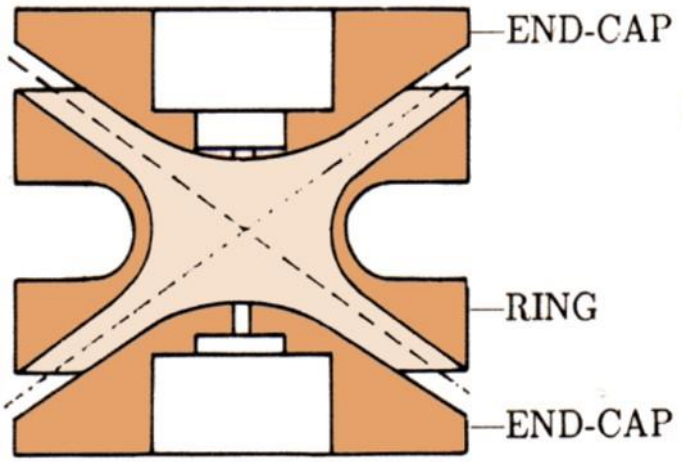

Figure 4 Schematic of the hyperboloidal ion trap
(http://static.sewanee.edu/physics/SEMINARS/HTML%20Griffith/sld004.htm)

The electric field generated by ac voltage applied on the ring electrode is expressed as

$$E_z = 2C_1 \frac{V_{ac} z}{z_0} (\cos \Omega t)\vec{k} \tag{2.5}$$

$$E_r = -C_1 \frac{V_{ac} r}{z_0} (\cos \Omega t)\vec{r} \tag{2.6}$$

where Ω is the frequency of the AC voltage, $\vec{k}$ and $\vec{r}$ are the unit vectors in the vertical and radial direction, $2\,z_0$ is the distance between the two endcap electrodes, E_z and E_r are electric field vectors in the vertical and axial directions, respectively. Since the geometry of the device is axisymmetric the electrical field component in the angular direction is 0. C_1 is geometric constant. For the classical bihyperboloidal configuration $C_1 = 1/z_0$, so Eq. 4.5 can be expressed as

$$E_z = 2V_{ac} \frac{z}{z_0^{\,2}} (\cos \Omega t)\vec{k} \tag{2.7}$$

From the expressions of electrical field induced by ac voltage, we can see the charged particle in the space surrounded by the electrodes is subject to periodic forces whose

strength are proportional to the distance from the center of the device. The electric field tha is produced by a dc voltage, V_{dc}, in the EDB device is

$$E_{dc} = C_0 \frac{V_{dc}}{z_0} \vec{k} \tag{2.8}$$

where C_0 is also a geometrical constant. In the electrical field of two infinitely large parallel plates the electrical field is uniform and C_0 is 1. While in the bihyperboidal configuration the electrical field is not uniform and the value of C_0 varies at different positions. Since the ac voltage is used to encounter the vertical forces when the particle is trapped in the nullpoint where the minimum electrical potential exists (the center of the device). The value of C_0 is important, which can be obtained by numerically solve the electrical field of the corresponding EDB configuration. Here the value of C_0 is assumed to be 1 from the expression of dc electrical field given in Davis, 1980. The dc electrical field at the nullpoint is expressed as

$$E_{dc} = \frac{V_{dc}}{z_0} \vec{k} \tag{2.9}$$

Suppose a charged particle is injected vertically from the center of the top endcap to a dynamic field. The trajectory of a charged particle with the mass of m and charge of q in the electrical filed are described as

$$\vec{F} = m\frac{d^2 z}{dt^2} = -C_d \frac{dz}{dt} + q\vec{E}_z - mg + q\vec{E}_{dc} + \vec{F}_z \tag{2.10}$$

and

$$m\frac{d^2 r}{dt^2} = -C_d \frac{dr}{dt} + q\vec{E}_r \tag{2.11}$$

where F_z are external forces such as the thermophoretic force , the photophoretic force and possibly, magnetic forces and so. We are not introducing any external forces here and $F_z = 0$ in our study, C_d is the drag coefficient and for a spherical particle it can be defined by

$$C_d = 3\pi d\mu \tag{2.12}$$

where d is the particle diameter, and μ is the viscosity of the gas phase.

Substitute equations 2.4, 2.6, 2.7 and 9 into equations 2.10 and 2.11, we have

$$m\frac{d^2z}{dt^2} = 2qV_{ac}\frac{z}{z_0^2}\cos\Omega t - \frac{qV_{dc}}{z_0} - 3\pi d\mu\frac{dz}{dt} - mg \tag{2.13}$$

$$m\frac{d^2r}{dt^2} = -3\pi d\mu\frac{dr}{dt} + qE_r \tag{2.14}$$

In the absence of external forces, the function of dc voltage thus becomes to overbalance the gravitational force.

$$-\frac{qV_{dc}}{z_0} = mg \tag{2.15}$$

Then Eq.2.13 becomes

$$m\frac{d^2z}{dt^2} = 2qV_{ac}\frac{z}{z_0^2}\cos\Omega t - 3\pi d\mu\frac{dz}{dt} \tag{2.16}$$

Equations 2.14 and 2.16 are second order nonlinear differential equations which are not easy to get analytical solution directly. Therefore the following nondimensional quantities are introduced,

$$\eta = \frac{z}{z_0} \tag{2.17}$$

$$R = \frac{r}{z_0} \tag{2.18}$$

$$\tau = \frac{\Omega t}{2} \tag{2.19}$$

We have

$$\frac{d^2\eta}{d\tau^2}+\left(\frac{6\pi\mu d}{m\Omega}\right)\frac{d\eta}{dt}-8\left(\frac{q}{m}\right)\left(\frac{V_{ac}}{\Omega^2 {z_0}^2}\right)\eta\cos(2\tau)=0 \tag{2.20}$$

$$\frac{d^2R}{d\tau^2}+\left(\frac{6\pi\mu d}{m\Omega}\right)\frac{dR}{dt}-4\left(\frac{q}{m}\right)\left(\frac{V_{ac}}{\Omega^2 {z_0}^2}\right)R\cos(2\tau)=0 \tag{2.21}$$

Apply transformations

$$\hat{\eta}=\eta e^{b\tau} \tag{2.22}$$

$$\hat{R}=\mathrm{R}e^{b\tau} \tag{2.23}$$

where $b=3\pi\mu d/m\Omega$, Equations 2.20 and 2.21 become

$$\frac{d^2\hat{\eta}}{d\tau^2}+\left(-b^2-8\left(\frac{q}{m}\right)\left(\frac{V_{ac}}{\Omega^2 {z_0}^2}\right)\cos(2\tau)\right)\hat{\eta}=0 \tag{2.24}$$

$$\frac{d^2\hat{R}}{d\tau^2}+\left(-b^2-4\left(\frac{q}{m}\right)\left(\frac{V_{ac}}{\Omega^2 {z_0}^2}\right)\cos(2\tau)\right)\hat{R}=0 \tag{2.25}$$

Rewrite the above two equations, eqs. 2.24 and 2.25

$$\frac{d^2\hat{\eta}}{d\tau^2}+\left(a-2q_z\cos(2\tau)\right)\hat{\eta}=0 \tag{2.26}$$

$$\frac{d^2\hat{R}}{d\tau^2}+\left(a-2q_r\cos(2\tau)\right)\hat{\eta}=0 \tag{2.27}$$

where $a=-b^2$, $q_z=2q_r=4\left(\frac{q}{m}\right)\left(\frac{V_{ac}}{\Omega^2 {z_0}^2}\right)$.Now we have the classical Mathieu Equation whose stability region has already been established. Figure 9 shows the stability region (enclosed by red lines) in parameter space of a and q_z. It has many separated regions; we can call the most left enclosed region stability region 1, the next stability region 2, etc. The solution in the r direction can be solved similarly. The stable region should be intersection of the both

directions. Compare equation (2.26) and (2.27), q_z is two times of q_r, which means the displacement in r direction is always stable as long as it is stable in z direction. Therefore the electrical field is adjusted to fulfill the stability in the z direction.

It should be noticed from equations 2.22 and 2.23 that the solutions of equations to the displacement is actually the product of the solution of Mathieu's equation and an exponentially decreasing term, therefore the stability region is expanded, which means some of the unstable region in Stability chart of Mathieu's equation is now stable due to the exponentially decreasing term. The details of the expanded stability region are derived in Appendix B.

If a particle is to be trapped in the nullpoint, it goes through a complicated trajectory before it is focused at the center. At a fixed time, if the electric field has coverage effect at the x direction, then it will have diverge effect at the z direction, and vice versa, but the overall effect is to focus the particle to the center after a complicated trajectory if we chose parameters to be at the overlapping region.

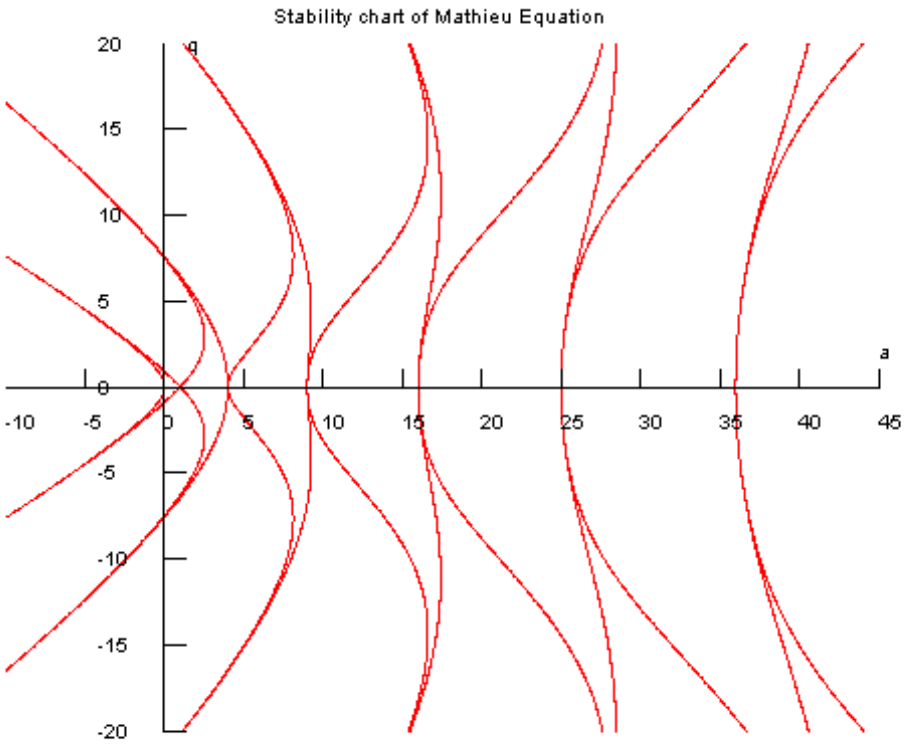

Figure 5 Stability chart of Mathieu Equation

2.3.2 Numerical approach to determine ideal operating conditions

From stability analysis in section 2.3.1 the parameters involved in determining whether trapped particles can stabilize in the nullpoint finally are V_{ac} , V_{dc} , Ω and charge mass ratio(q/m). It does not take the maximum displacement the particle can travel nor the time needed to stabilize into account. Besides satisfying the stability criteria the trapped particle should always remain inside the chamber, which means the maximum displacement the particle could travel should be less than the minimum dimension of the center to the wall of the trapping system. Furthermore once the particle is injected to the trapping system the time needed to stabilize the particle in the center also matters for some time consuming

experiment such as evaporation, reaction and combustion process. We are interested in studying the evaporation of micro sized liquid droplet. The lifetime of the droplet in our study is around a few seconds, and our goal is to study the evaporation process from the initial injected droplet. Therefore reducing the response time in trapping the droplet is important.

For the above reasons, we adopted the numerical simulation approach to solve the 2^{nd} order differential equation (2.7) with proper initial conditions. The Matlab code solving this problem is provided in Appendix C. The trajectories of ethanol and glycerol droplets with size of 10μm and 100 μm are studied under different induced velocities. The charge ratio of all the cases discussed below is 70% Raleigh limit.

The droplet is injected from the top of the four rings EDB setup right through the axis of the rings. The droplet vibrates up and down under the ac electrical field and will finally stabilize in the center point when dc is set to overbalance gravity and ac voltage and frequency was set to satisfy the stability criteria. The separation distance of ac rings is 6 mm, so the displacement should always be within the -3~3 mm during the vibration process. The simulation results shows that for a 100 μm droplet with induced velocity larger than 2 m/s the droplet can easily go out of the rings even it will stabilize finally.

Figures 10~13 list the trajectories of 100 μm droplet under various induced velocities. The droplet can go up to 10 mm under 0.7 m/s. By reducing the velocity the maximum displacement can be reduced, the droplet is maintained between the space of ac rings once the velocity (u) is 0.01 m/s. The figures also show the response time to stabilize droplet decreases as velocity decreases. Figure 11 shows the trajectory of a 100 μm droplet under the velocity of 3 m/s we can see the maximum displacement is around 7.5 mm, which is less

than that of a larger droplet (100 μm) under 0.7 m/s. From the above analysis we can conclude that the bigger droplet size needs much smaller velocity to help maintain the droplet within the EDB setup and reduce the response time to get stabilized. Since the droplet velocity from ES is usually larger than 3 m/s, the velocity should be damped before reaching the EDB setup. In our work extra upward electrical field is applied to reduce the droplet induced velocity, the detailed information will be discussed in section 2.4.

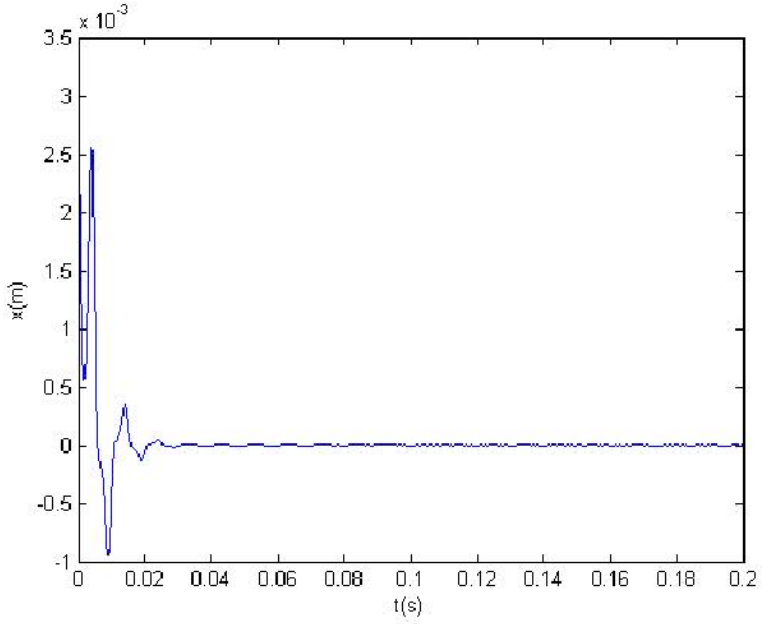

Figure 6 Trajectory of droplet in the vertical direction with d=100μm, Ω =1256rad/s, V_{ac} =2000V,u=0.01m/s

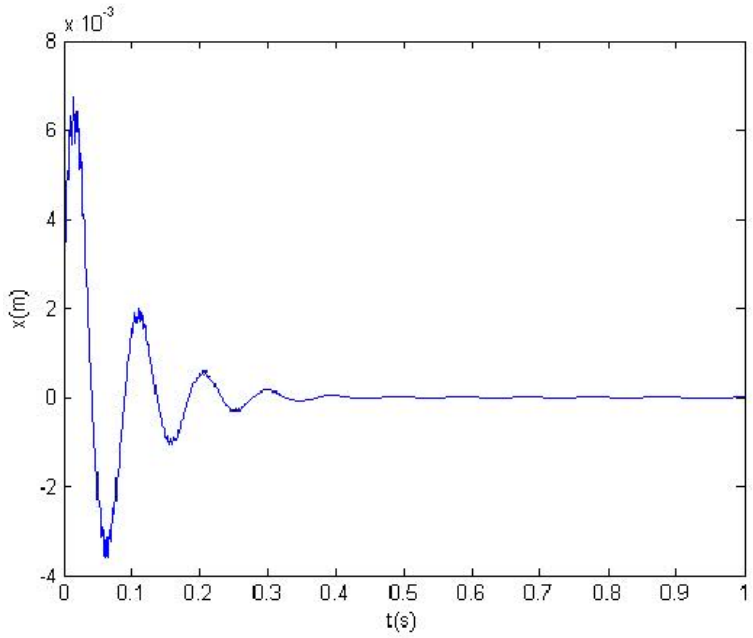

Figure 7. Trajectory of droplet in the vertical direction with d=100μm, Ω =1256r0ad/s, V_{ac} =2000V, u=0.4m/s

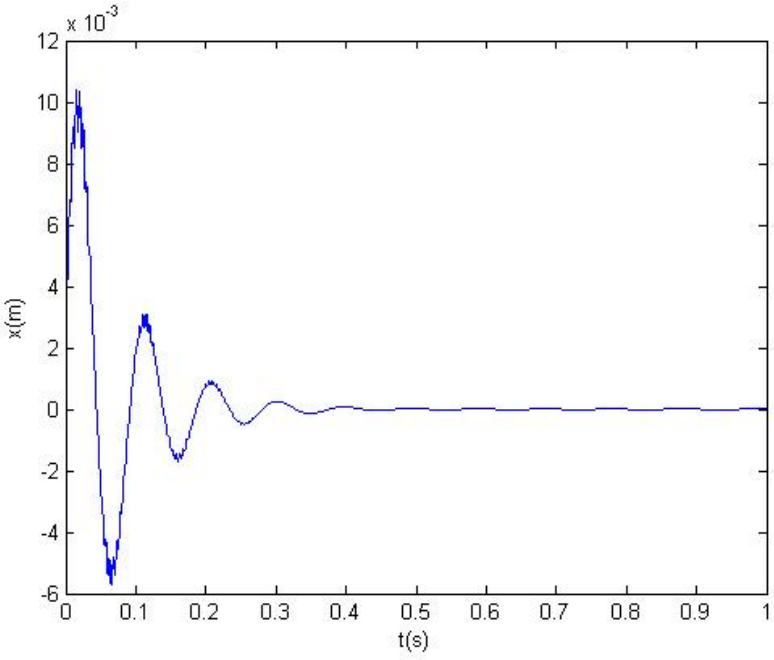

Figure 8. Trajectory of droplet in the vertical direction with d = 100 μm, Ω = 1256 rad/s, V_{ac} = 2000 V, u = 0.7 m/s

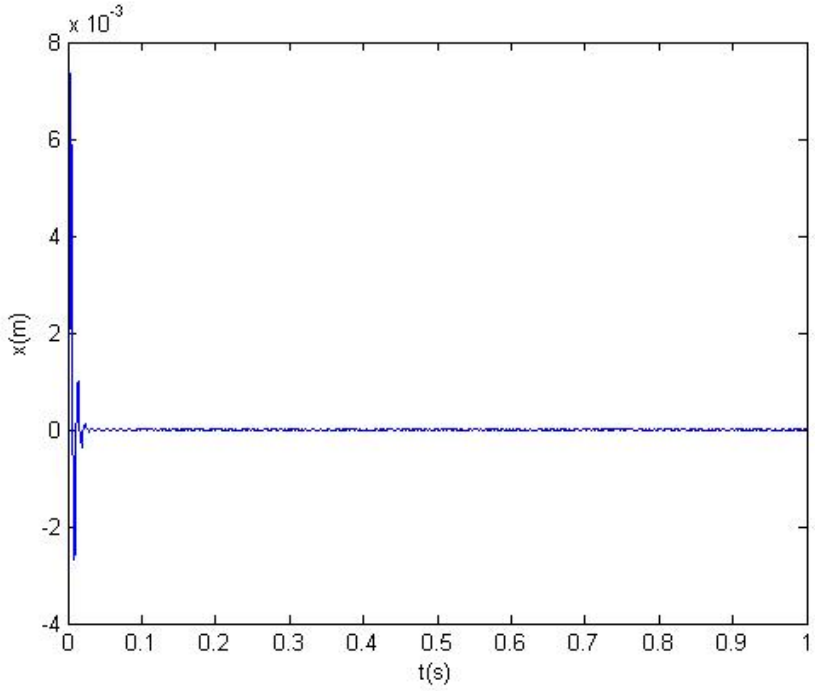

Figure 9. Trajectory of droplet in the vertical direction with $d = 10$ μm, $\Omega = 1256$ rad/s, $V_{ac} = 2000$ V, $u = 3$ m/s

2.3.3 Theory of double rings EDB device

Although the classical configuration of the device is the bihyperboloidal chamber, many other configurations that are much easier to build have been developed as described in the introduction part in chapter 2.3. For the simplicity of construction and also feasibility for optical device, we adopted the simplest configuration developed by Weiss-Wrana, 1983, Ray and Souyri, 1989 and Davis, 1990. The ac and dc electrodes are replaced by four parallel rings. Figure 14 shows the geometry and circuitry. The top and bottom rings are connected to dc voltage. The relative potential difference is determined by the polarity of the charged droplet. In our study the droplet has positive charge, so the higher potential should be connected to bottom ring to induce upward electrical field. The middle rings are connected to ac voltage and the other end of the ac voltage is connected to the ac circuit with the

potential of $V_{ac}/2$. In our experiment the point is connected to ground with 0 potential, therefore the potentials of top and bottom rings become $-V_{ac}/2$ and $V_{ac}/2$, respectively. Analytical solution of the electrical field is provided in Davis, 1990.

$$E_{ac,z} = \frac{\pi V_{ac} \cos wt}{\psi(\xi_1, \xi_2)(R^2 + h^2)^{3/2}} z \tag{2.28}$$

$$E_{dc,z} = \frac{\pi V_{dc} z_0}{\varphi(\xi_3, \xi_4)(R^2 + {z_0}^2)^{3/2}} \tag{2.29}$$

where R is distance of the center point to electrodes, h and z_0 are the distances from the center point to the ac and dc electrodes, $\psi(\xi_1, \xi_2)$ and $\varphi(\xi_1, \xi_2)$ are geometrical parameters which are expressed as

$$\psi(\xi_1, \xi_2) = \frac{K(\xi_1)}{2R} + \frac{K(\xi_2)}{2(R^2 + h^2)^{1/2}} \tag{2.30}$$

$$\varphi(\xi_3, \xi_4) = \frac{K(\xi_3)}{2R} - \frac{K(\xi_4)}{2(R^2 + {z_0}^2)^{1/2}} \tag{2.31}$$

Where $K(\xi_1)$, $K(\xi_2)$, $K(\xi_3)$ and $K(\xi_4)$ are the complete elliptic integrals of the first kind. The function of $K(k)$ has the simplified approximation

$$K(k) = \frac{\pi}{2}\left\{1 + \left(\frac{1}{2}\right)^2 k^2 + \left(\frac{1 \cdot 3}{2 \cdot 4}\right)^2 k^4 + \cdots + \left[\frac{(2n-1)!!}{(2n)!!}\right]^2 k^{2n} + \cdots\right\} \tag{2.32}$$

The precision of the aproximation is smaller than 3×10^{-4} for $k < 1/2$. ξ_1, ξ_2, ξ_3 and ξ_4 have the following forms

$$\xi_1 = \xi_3 = 1 - t^2 / 4R^2 \tag{2.33}$$

$$\xi_2 = 1 - (t^2 + 4h^2)/(4R^2) \tag{2.34}$$

$$\xi_4 = 1 - (t^2 + 4{z_0}^2)/(4R^2) \tag{2.35}$$

where t is the radius of the ring electrode. Compared to the electrical field in classical bihyperboidal geometry (eqs. 2.5 and 2.7), eq.2.28 can also be written as the form of

$$E_{ac,z} = \frac{\pi V_{ac} \cos wt}{\psi(\xi_1, \xi_2)(R^2 + h^2)^{3/2}} z = 2C_1 V_{ac} \frac{z}{h} \cos wt \qquad (2.36)$$

where geometric constant of $C_1 = \pi h / 2(\psi(\xi_1, \xi_2)(R^2 + h^2)^{3/2})$, Similar to analogy in ac electrical field eq. 2. 29 can be written as

$$E_{dc,z} = \frac{\pi V_{dc} z_0}{\varphi(\xi_3, \xi_4)(R^2 + {z_0}^2)^{3/2}} = C_0 \frac{V_{dc}}{z_0} \qquad (2.37)$$

where $C_0 = \pi {z_0}^2 / (\varphi(\xi_3, \xi_4)(R^2 + {z_0}^2)^{3/2})$. The only differences of the electrical fields between classical bihyperboloidal and four rings configurations are the geometrical constants. The theoretical analysis in section 2.3.2 is also applicable for the four ring configuration.

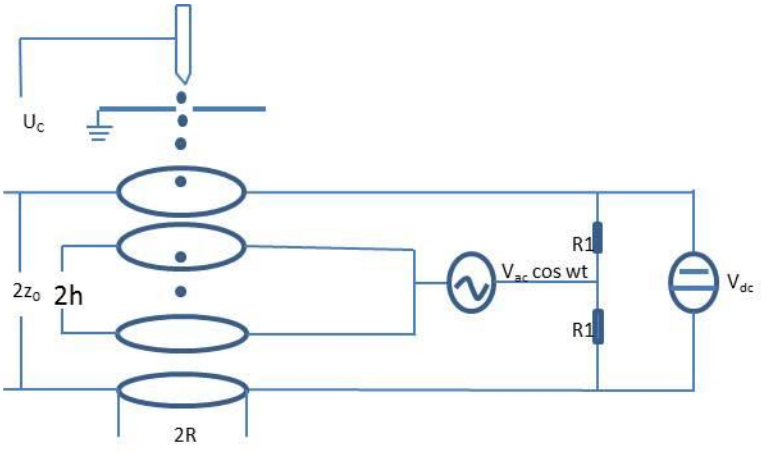

Figure 10 Configuration of the double-ring electrodynamic balance

The values of C_0 and C_1 can also be obtained with the numerical approach by solving the Laplace. For the boundary condition we use the dimension of the experimental setup (details will be shown in section 2.4), the four rings have the same dimension, the radius of the ring electrode (t) is 1.15 cm. The distance between the ring center and the electrode (R)

is 11.35mm. The separation distance of the middle ac electrodes ($2h$) is 6 mm. The distance of the two dc electrodes ($2z_0$) is 25 mm. The simulation is implemented in COMSOL. The origin of the 2-d cylindrical coordinate is set to be at the center point of the EDB setup. When calculating the electrical field induced by ac voltage, the potential of dc electrodes were set to be 0. From eq.2-29 we can see the relation between the electrical field and the z coordinates is linear at any time. To get the constant value (C_1), we only need to apply a potential to the ac electrodes and get the plot of vertical electrical vs. coordinates, the slope of the plot is $2C_1 / h$. The ac electrodes were set to be 2000 K. Figure 14 shows the electrical field in the z direction. It shows the electrical field can be approximated to be linear between the two ac rings (-0.003-0.003m) (shown in Figure 15).

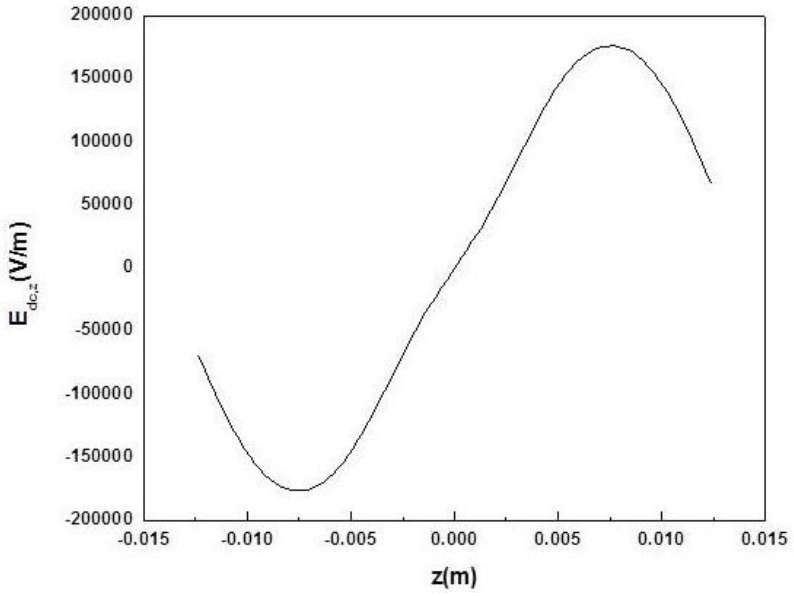

Figure 11 Vertical electrical field at V_{ac}=2,000 V

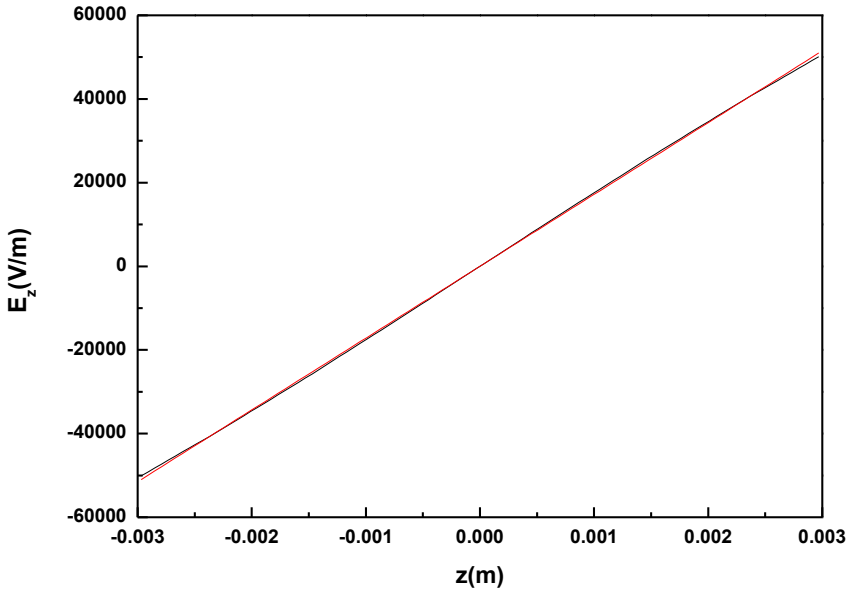

Figure 12 Zoom in picture of vertical electrical field between ac rings at V_{ac}=2,000 V

2.4 Droplet visualization

To image the micro droplet with highest possible optical resolution (i.e. only limited by the Abbe diffraction limit), great care needs to be taken on the design of the visualization subsystem. The challenges come from two aspects: first, the high AC voltage of the EDB; second, the motion blur caused by the combined high magnification rate and hovering motion of the droplet.

We used a 10x long working distance microscope lens (Edmund Optics EO M Plan Apo infinity-corrected) to allow sufficient distance away from the charged metal rings. The working distance of the lens is 33.5mm, with a focal length of 20mm. The Numerical Aperture NA is 0.28. The diffraction limit states:

$$d = \lambda_L / 2NA \tag{2.38}$$

where d is the resolution limit, λL is the light source wavelength. This suggests that with typical visible light wavelength of 540nm (green light), the resolving power of the lens is ~

1μm. It also suggests that shorter wavelength will result in slightly higher resolution. In addition, the light source should be nearly monochromatic to minimize chromatic dispersion. Because of these considerations, we choose a high power blue LED as the light source, which is collimated into approximately parallel beam.

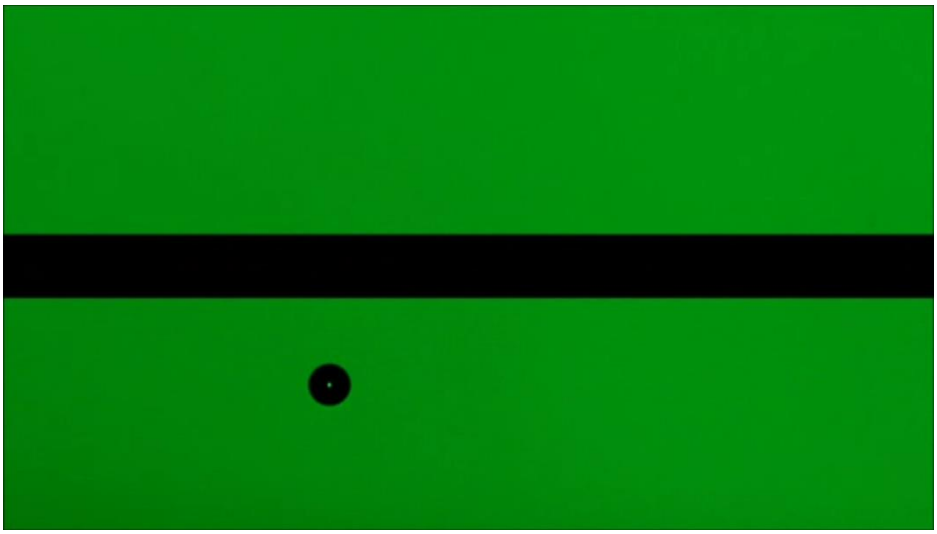

Figure 13 Single levitated evaporating ethanol droplet

The camera we used is a Canon 650 DSLR. The sensor size of the camera is 22.3 ×14.9 mm, and the pixel number is 5184 ×3456 with the pixel size of 4.3 ×4.3μm. To ensure each pixel matches the revolving power of the lens (~1μm), we added extension tube adapter to the lens and achieved 8.3x effective optical magnification.

The droplet will not be absolutely still in the EDB. The typical hovering speed of the droplet is about 5 cm/s. With 8x magnification, the image moving speed is 40cm/s. To avoid motion blur, an exposure time should guarantee the image does not shift more than half of a pixel, or ~5μs. This value is unachievable by the camera. Instead, we strobe the LED light with short pulse of ~1μs. The LED is driven by a pulse generator, which is triggered by a function generator set at 29.97 Hz (same frequency of the video mode of the camera). Note that if the

triggering frequency is not synchronize as the video mode of the camera, a rolling fringe artifact will appear on the video footage (shown in Figure 17).

2.5 The completed experimental apparatus

The complete experimental setup is shown in Figure 18, which consists of the subsystems previously described: droplet generation, droplet injection, droplet levitation, and visualization.

The atomizer is a stainless steel needle charged at positive high voltage V_1. The top plate of the injector (or extractor) is connected to negative high voltage ($-V_2$). Electrospray is generated by the voltage difference between the nozzle and the extractor ($V_1 + V_2$). After the extracted jet go through the hole (3 mm) right below the needle the jet breaks up into droplets with a certain velocity, as shown in Figure 18. The injection component and EDB are mounted on a 2-d stage to allow easy alignment. The two systems are connected with the metal rods with plastic screws on the connection parts for insulation.

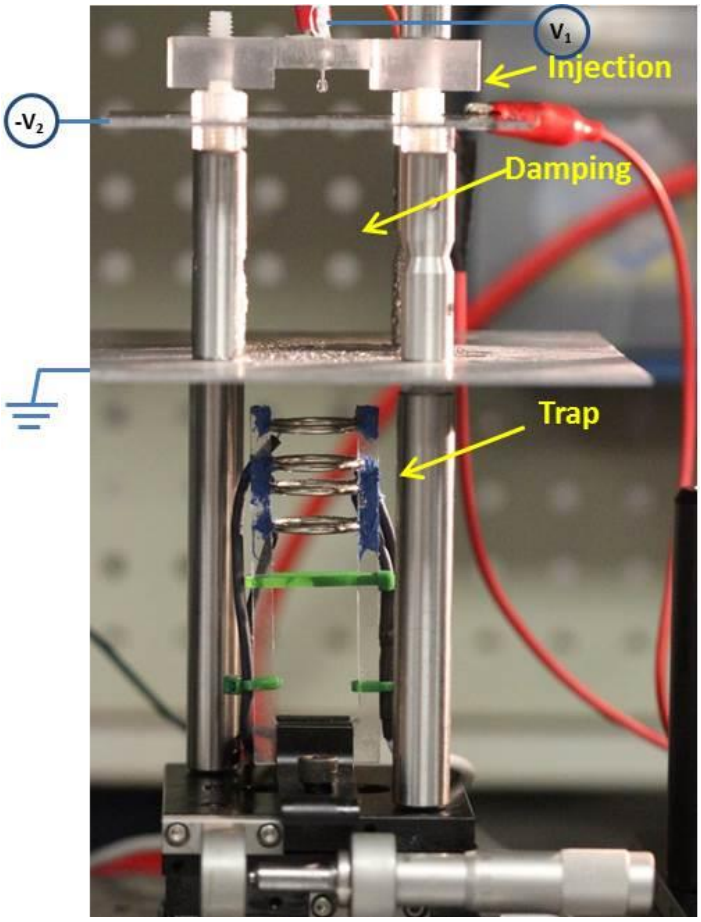

Figure 14. Experimental setup

As discussed in section 2.2 the velocity of the droplets should be reduced before entering the EDB. The injection system is formed by two parallel Alumina plates, one is used as extractor in ES system with the dimension of 2 inches ×2 inches, the other is used as ground with the dimension of 4 inches × 4 inches (shown in Figure 18). The grounded plate separates the electrical field in the damping system and that in the EDB. The reason for the lager ground plate is that the spray profile is developing as it propagates, and the radius of cross section is approximately proportional to the square root of distance it travels. The separation distance of the two plates is 2 inches, so the grounded plate has the dimension of 4 inches ×4 inches. There is one hole on the plate with the radius of 3 mm, which allows very

few droplets to go through. The holes on the two plates are aligned with the center of the trapping system. There is an upward electrical field to damp the droplet velocity. $-V_2$ can be adjusted to make most of the droplet fly back while still allows few to go through the hole in the grounded plate.

Figure 19 shows the spray profile in the injection section. Compared to Figure 20 most droplets fly upward and only a few droplets can go through the holes on the bottom plate to the trapping system. Figure 21 shows the droplet injection velocities into the trapping systems under various negative high voltages. The velocity decreases as voltage increases. As discussed in section 2.3.3 smaller velocity is good for trapping.

The four rings are inserted to a machined support to make the four rings coaxial. The support is fixed right below the grounded plate. Therefore once the droplet goes through the grounded plate it can be levitated.

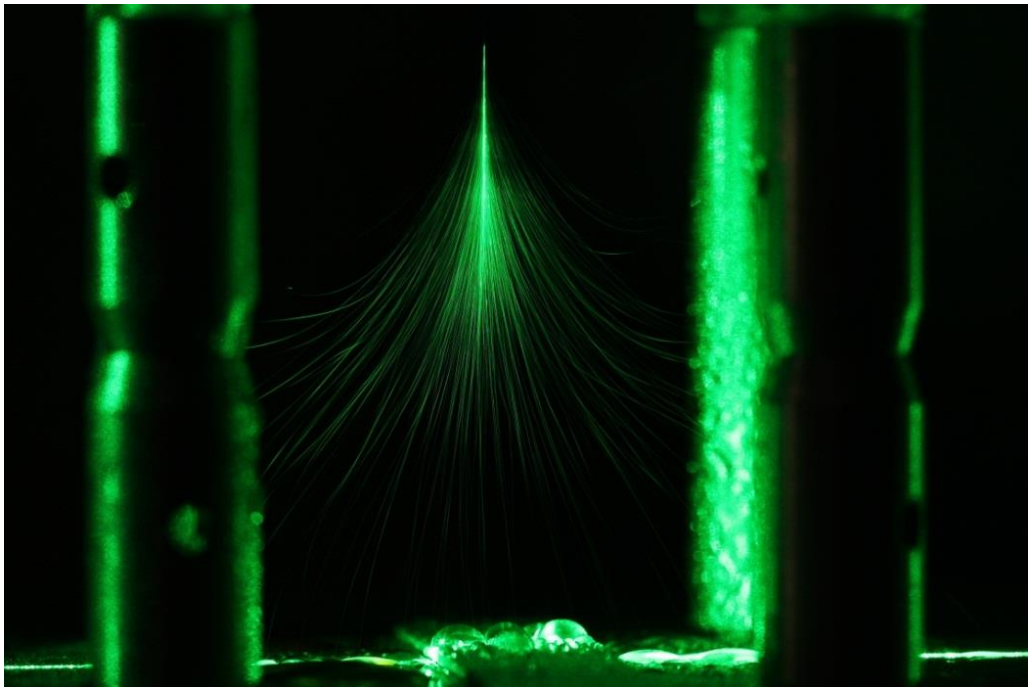

Figure 15. Electrospray profile of glycerol under cone jet mode with the flow rate of 2 ml/h without damping system

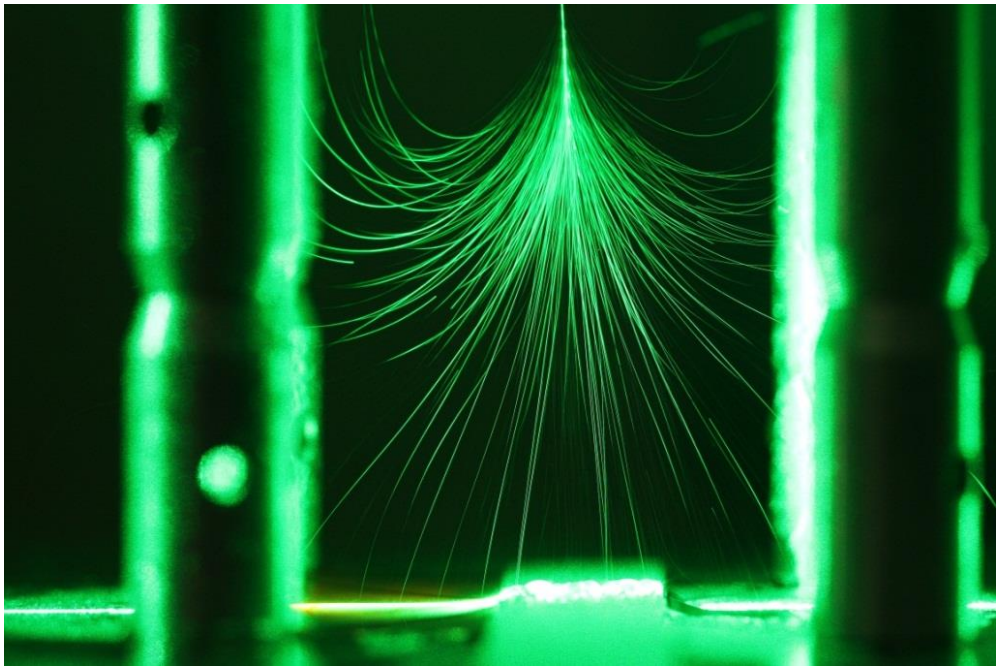

Figure 16 Electrospray profile of glycerol under cone jet mode with the flow rate of 2 ml/h with damping system by setting $-V_2$ = -0.943 kV

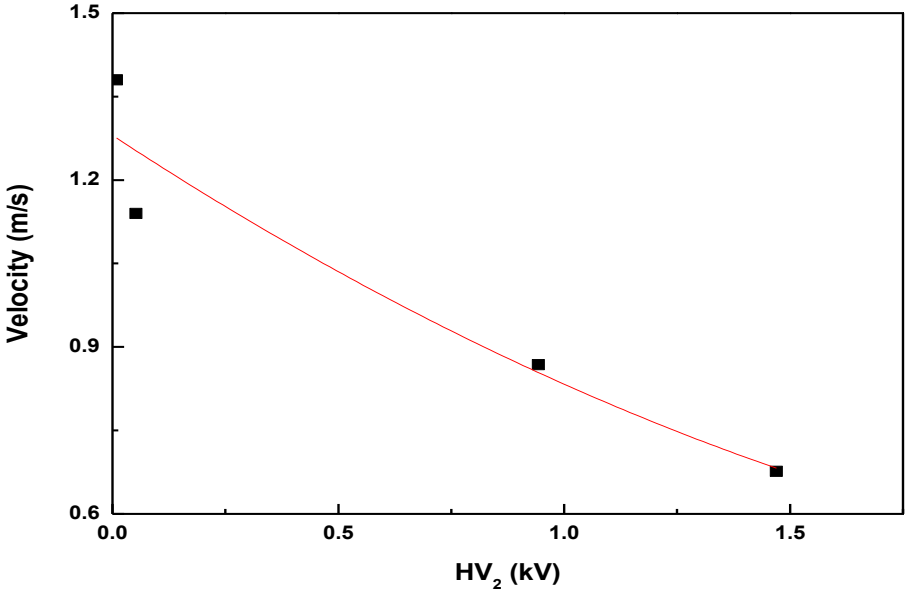

Figure 17 Droplet injection velocities under different electrical field

2.6 Performance of the experimental apparatus

We have successfully generated, injected, levitated, and imaged microdroplets of glycerol, water, and water+ethanol mixture. Figure 22 (a) shows the still image of the levitated micro glycerol droplet. The droplet size is measured through counting the number of pixels. The uncertainty is ± 0.52 μm.

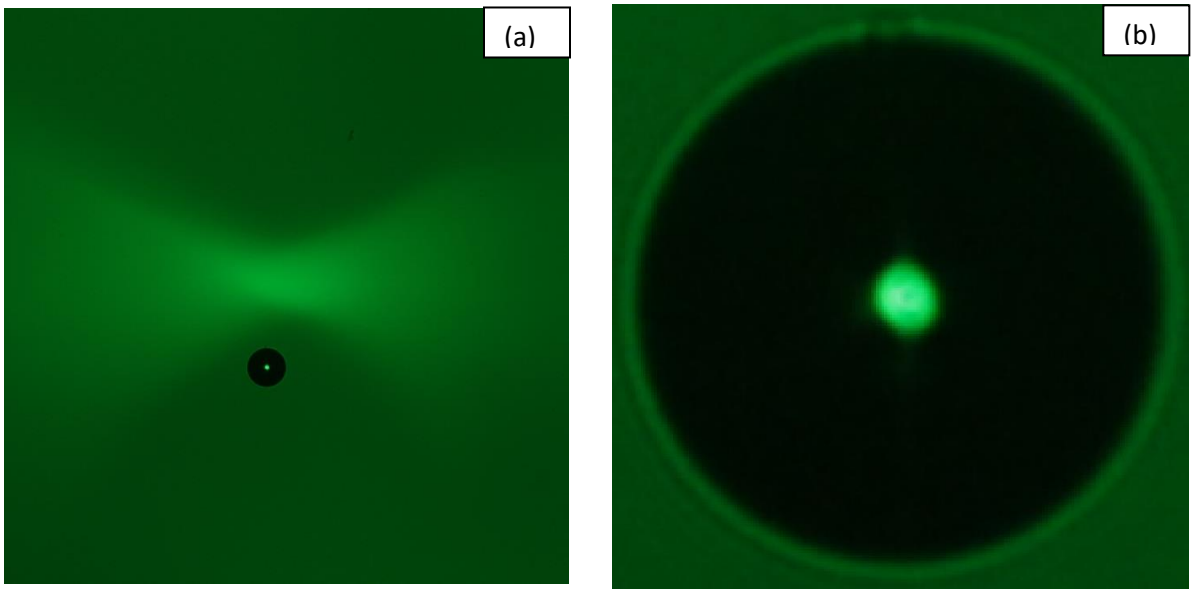

Figure 18 Microdrop imaging. (a) Direct zoom lens image. (b) Magnified image of 102 μm droplet

Because the video recording frame rate is 30 Hz, and the typical droplet evaporation time (100μm) is ~3 seconds, the complete evaporation even can be capture with 100 or more frames, which are adequate for both qualitative and qualitative investigation. For example, Figure 23 shows the image sequence of the complete evaporation history of a 90 μm water droplet with 178 images which allow full characterization of the droplet size change history.

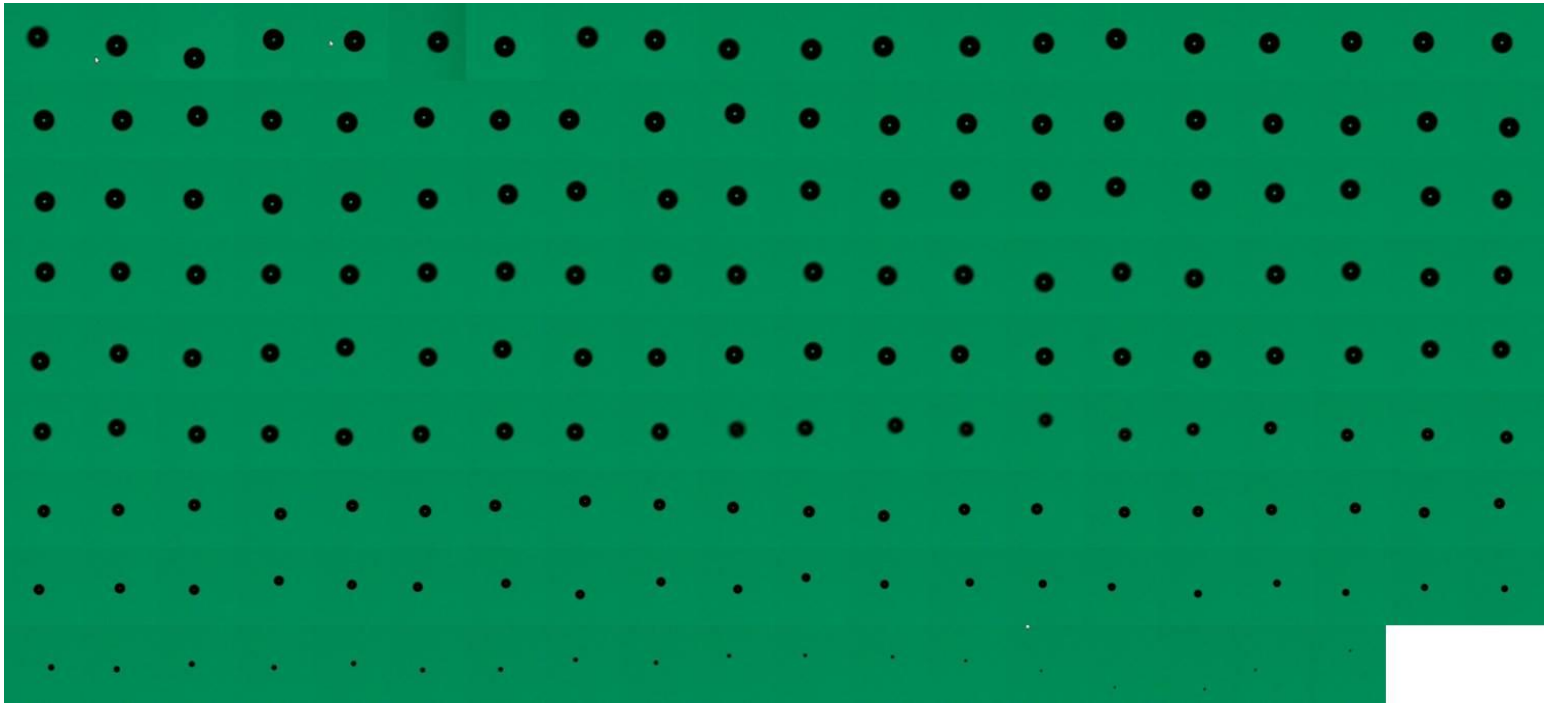

Figure 19 Complete evaporation history of a micro water droplet

Figure 24 shows the typical behavior of pure DI water, which closely follows D^2-law. This suggests our experimental setup is a powerful tool to study the evaporation of microdroplets.

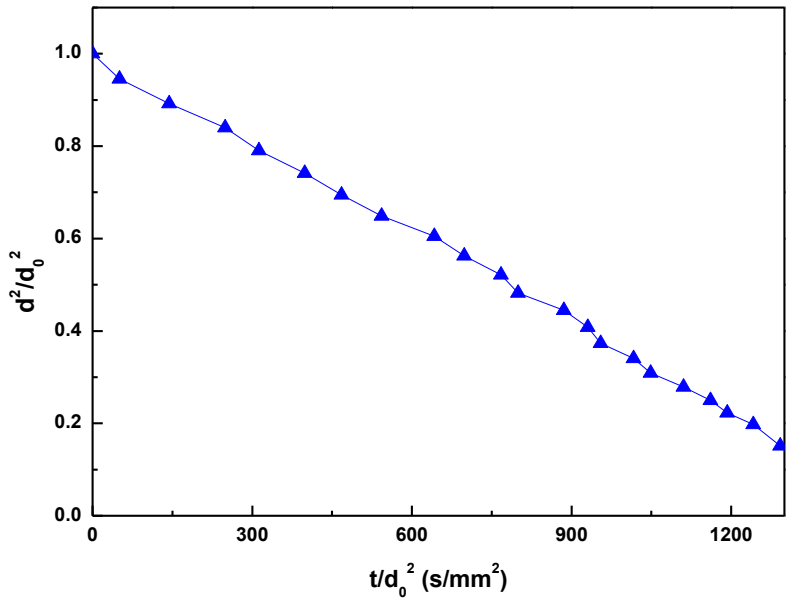

Figure 20 Droplet size history of a evaporating micro water droplet

APPENDIX B: SOLUTION TO MATHIEU'S EQUATION

The Mathieu's equation is defined by:

$$\frac{d^2x}{d\xi^2} + (a - 2q\cos 2\xi)x = 0 \qquad \text{(B.1)}$$

The solution to Mathieu's equation is written as:

$$x = \alpha' e^{\mu\xi} \sum_{n=-\infty}^{+\infty} C_{2n} e^{2in\xi} + \alpha'' e^{-\mu\xi} \sum_{n=-\infty}^{+\infty} C_{2n} e^{-2in\xi} \qquad \text{(B.2)}$$

where α' , α'' are integration constants, whichdepends on the initial conditions, C_{2n} and μ depend on the values of a and q. Stable solutions are those where x remains finite as $\xi \to \infty$. Whether a solution is stable or not depends on the value of μ, as μ is only dependent on the values of a and q, the stability region of Mathieu's Equation on depends on these two values but not on the initial conditions.

There are four possibilities for μ:

(1) μ is real and non-zero. Instability arises from the $e^{\mu\xi}$ or $e^{-\mu\xi}$ factor.

(2) $\mu = i\beta$ is purely imaginary and beta is not an integer. These solutions are stable.

(3) μ is a complex number, the solutions are unstable.

(4) $\mu = im$ is purely imaginary and m is an integer. The solutions are periodic but unstable. $\mu = im$ corresponds to a curve in the (a, q) space when m is an integer, the curves forms the boundaries between the stable and unstable regions .

If we plug solution (A.2) in to Mathieu Equation (A.1), we get the recurrence

$$[a + (\mu + 2in)^2]C_{2n} - qC_{2n-2} - qC_{2n+2} = 0 \qquad \text{(B.3)}$$

Let $\rho_n = (\mu + 2in)^2 + a$, equation (B.3) becomes:

$$\frac{-q}{\rho_n}C_{2n-2}+C_{2n}-\frac{q}{\rho_n}C_{2n+2}=0 \tag{B.4}$$

To get a nontrivial solution, the determinant of the above simultaneous equations (shown below) must be zero:

$$\Delta(\mu)=\begin{vmatrix}
\cdots & \cdots & \cdots & \cdots & \cdots & \cdots & \cdots & \cdots & \cdots \\
0 & \frac{-q}{\rho_{-2}} & 1 & \frac{-q}{\rho_{-2}} & 0 & \cdots & \cdots & \cdots & \cdots \\
\cdots & 0 & \frac{+q}{\rho_{-1}} & 1 & \frac{-q}{\rho_{-1}} & 0 & \cdots & \cdots & \cdots \\
\cdots & \cdots & 0 & \frac{+q}{\rho_0} & 1 & \frac{-q}{\rho_0} & 0 & \cdots & \cdots \\
\cdots & \cdots & \cdots & 0 & \frac{-q}{\rho_1} & 1 & \frac{+q}{\rho_1} & 0 & \cdots \\
\cdots & \cdots & \cdots & \cdots & 0 & \frac{-q}{\rho_2} & 1 & \frac{-q}{\rho_2} & 0 \\
\cdots & \cdots & \cdots & \cdots & \cdots & \cdots & \cdots & \cdots & \cdots
\end{vmatrix} \tag{B.5}$$

Set $\Delta(\mu)=0$, which is equivalent to:

$$\sin^2[(\pi i\mu)/2]=\Delta(0)\sin^2[(\pi\sqrt{a})/2] \tag{B.6}$$

Let $\mu=\gamma+in, n\in N$, we have:

$$\sin[i\frac{\pi}{2}(\gamma+in)]=i\sinh(\frac{\pi}{2}\gamma)\cos(\frac{\pi}{2}n)-\cosh(\frac{\pi}{2}\gamma)\sin(\frac{\pi}{2}n) \tag{B.7}$$

There are two cases for *n*:

(1) *n=2m*, we have:

$$\cos(\frac{\pi}{2}n)=(-1)^m, \sin(\frac{\pi}{2}n)=0 \tag{B.8}$$

Thus

$$\Delta(0)\sin^2(\frac{\pi}{2}\sqrt{a})=-\sinh^2(\frac{\pi}{2}\gamma) \tag{B.9}$$

(2) *n=2m+1*, we have:

$$\Delta(0)\sin^2(\frac{\pi}{2}\sqrt{a})=\cosh^2(\frac{\pi}{2}\gamma) \tag{B.10}$$

To get the expanded stability region of the problem discussed in Chapter 4.3.1, we set $\gamma=K$, and then equation (B.9) (B.10) forms the boundaries between stable and unstable regions. To get the stability region to the classical Mathieu's equation,

we set $\gamma = 0$ and equation (B.9) (B.10) forms the boundaries between stable and unstable regions. These regions can only be determined numerically as we are dealing with an infinitely large determinant. The stability region of the Mathieu's equation is shown in Figure 50.

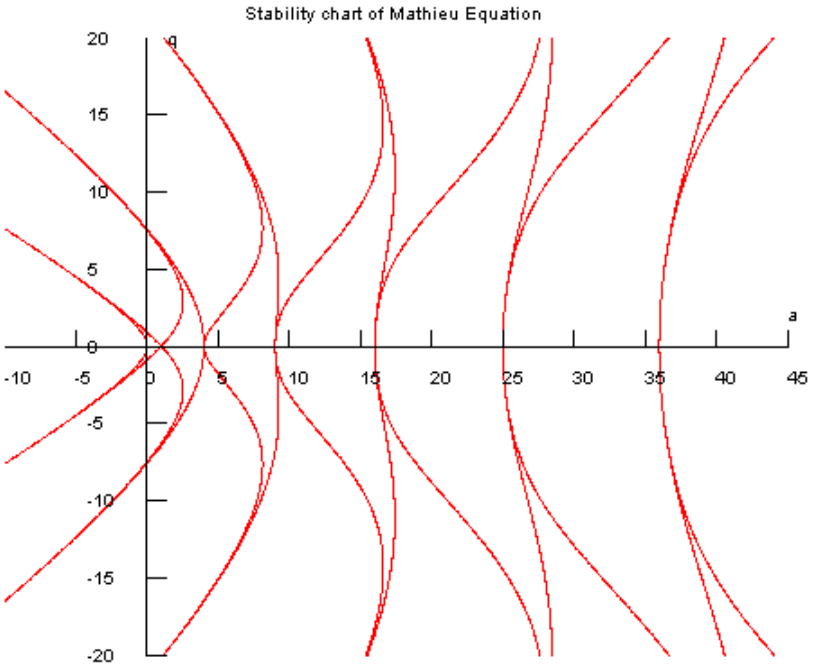

Figure 21 Stability of Mathieu's equation

As can be observed from the stability region of Mathieu's equation, $(a,q)=(n^2,0)$ is the separation point of adjacent stable regions, which can be verified by plugging in the value of $(a,q)=(n^2,0)$ to equation(B.5) and setting $\mu = in$.

For our problem discussed in Chapter 4.2,1 $a = -K^2 = -(\frac{3\pi\eta d}{mw})^2 < 0$, therefore only the left half plane of the stability region can be used.

Approximate analytical solutions can be obtained by truncating the infinite determinant (B.5) to 3×3, 5×5, 7×7 orders. The dashed lines in equation (B.5) show the 3×3 and 5×5 determinant. The first three of these determinants are shown below:

$$\Delta_1(0) = 1 + \frac{2q^2}{(4-a)a} \tag{B.11}$$

$$\Delta_2(0) = \frac{2q^2\left(1-\frac{q^2}{(4-a)(16-a)}\right)}{(4-a)a} + \left(1-\frac{q^2}{(4-a)(16-a)}\right)^2 \tag{B.12}$$

$$\Delta_3(0) = 2q^2\left(1-\frac{q^2}{(16-a)(35-a)}\right)\left[\frac{\left(1-\frac{q^2}{(4-a)(16-a)}-\frac{q^2}{(16-a)(36-a)}\right)}{(4-a)a}\right] + \left(1-\frac{q^2}{(4-a)(16-a)}-\frac{q^2}{(16-a)(36-a)}\right)^2 \tag{B.13}$$